Chemical Science

ROYAL SOCIETY OF CHEMISTRY

EDGE ARTICLE

View Article Online
View Journal | View Issue

Check for updates

Cite this: *Chem. Sci.*, 2020, **11**, 4381

All publication charges for this article have been paid for by the Royal Society of Chemistry

# What is the role of acid–acid interactions in asymmetric phosphoric acid organocatalysis? A detailed mechanistic study using interlocked and non-interlocked catalysts†‡

Dennis Jansen,[a] Johannes Gramüller,[b] Felix Niemeyer,[a] Torsten Schaller,[a] Matthias C. Letzel,[c] Stefan Grimme,[d] Hui Zhu,*[d] Ruth M. Gschwind*[b] and Jochen Niemeyer*[a]

Organocatalysis has revolutionized asymmetric synthesis. However, the supramolecular interactions of organocatalysts in solution are often neglected, although the formation of catalyst aggregates can have a strong impact on the catalytic reaction. For phosphoric acid based organocatalysts, we have now established that catalyst–catalyst interactions can be suppressed by using macrocyclic catalysts, which react predominantly in a monomeric fashion, while they can be favored by integration into a bifunctional catenane, which reacts mainly as phosphoric acid dimers. For acyclic phosphoric acids, we found a strongly concentration dependent behavior, involving both monomeric and dimeric catalytic pathways. Based on a detailed experimental analysis, DFT-calculations and direct NMR-based observation of the catalyst aggregates, we could demonstrate that intermolecular acid–acid interactions have a drastic influence on the reaction rate and stereoselectivity of asymmetric transfer-hydrogenation catalyzed by chiral phosphoric acids.

Received 20th February 2020
Accepted 1st April 2020

DOI: 10.1039/d0sc01026j

rsc.li/chemical-science

Open Access Article. Published on 07 2020. Downloaded on 07/01/2026 18:02:33.
This article is licensed under a Creative Commons Attribution-NonCommercial 3.0 Unported Licence.

## Introduction

Many organocatalysts, such as amines, diols, amino-acid derivatives, (thio)ureas or phosphoric acids are highly functionalized organic molecules, oftentimes featuring hydrogen-bond donor and acceptor moieties or even Brønsted-acidic and Brønsted-basic functional groups within the same molecule.[1] Also, many organocatalytic reactions rely on the use of high catalyst loadings and are performed in aprotic organic solvents.[2–4] This makes the formation of aggregates highly likely, be it catalyst·catalyst aggregates or higher-order catalyst·catalyst·substrate aggregates. The comprehension and control of such aggregation processes would not only enable a better understanding of organocatalytic processes, but also open up new possibilities in catalysis, when such catalyst aggregates can be designed and applied in a controlled fashion.

In previous studies, aggregation of organocatalysts was observed in a few cases: in urea-catalysis, Jacobsen has shown that catalyst–catalyst interactions can be both detrimental and beneficial.[5] The identification of cooperative substrate activation in a catalyst·catalyst·substrate complex led to the development of tethered[6] and macrocyclic[7] bis-urea catalysts. Supramolecular catalyst aggregation has also been observed for chincona-alkaloid based organocatalysts, in this case leading to catalyst deactivation and decreased enantioselectivities.[8] In the case of BINOL-based phosphoric acids,[9] Gong showed that acid–acid interactions lead to a different solubility of the racemic and homochiral catalyst species, resulting in strong nonlinear effects.[10] Phosphoric acid aggregation has also been proven by spectroscopic means: dimers and trimers of dimethylphosphoric acid were identified by NMR[11] and Hunger could show the presence of multimers for complexes of diphenyl phosphoric acid and a quinoline.[12] For chiral phosphoric acids (CPA) with a BINOL-backbone, extended aromatic surfaces allow additional weak non-covalent interactions, which further stabilize hydrogen-bonded catalyst·substrate complexes,[13,14] and can also enable the formation of higher aggregates, such as dimers of CPA·imine complexes.[15]

We recently found that integration of two BINOL-phosphoric acids in a catenane structure[16] leads to drastic changes both in

[a]Faculty of Chemistry (Organic Chemistry) and Center for Nanointegration Duisburg-Essen (CENIDE), University of Duisburg-Essen, Universitätsstrasse 7, 45141 Essen, Germany. E-mail: jochen.niemeyer@uni-due.de

[b]Organic Chemistry, University of Regensburg, 93040 Regensburg, Germany

[c]Institute of Organic Chemistry, University of Münster, Corrensstrasse 40, 48149 Münster, Germany

[d]Mulliken Center for Theoretical Chemistry, Rheinische Friedrich-Wilhelms Universität Bonn, Beringstrasse 4, 53115 Bonn, Germany

† In memory of Prof. Carsten Schmuck.

‡ Electronic supplementary information (ESI) available. See DOI: 10.1039/d0sc01026j

Open Access Article. Published on 07 2020. Downloaded on 07/01/2026 18:02:33.
This article is licensed under a Creative Commons Attribution-NonCommercial 3.0 Unported Licence.

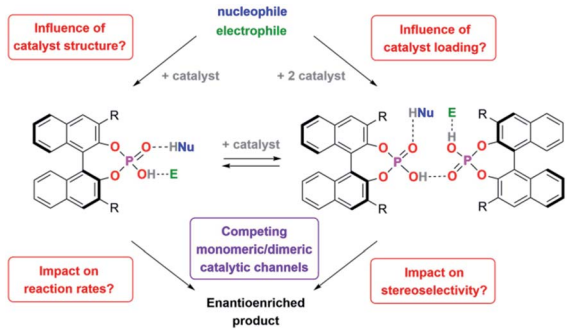


Scheme 1 Key questions for this investigation.

reaction rates and stereoselectivities for the transfer-hydrogenation of quinolines. DFT-calculations suggested that a hydrogen-bond mediated acid–acid interaction[17,18] leads to a more stereoselective dimeric catalyst pathway (featuring two acids and both substrates), as opposed to a less stereoselective monomeric pathway (involving one acid and both substrates).

We thus concluded that the mechanical interlocking of two phosphoric acids is an effective means to channel the reaction through the dimeric pathway, but of course other factors that lead to increased acid–acid interactions (such as higher catalyst loadings) might have a similar effect (Scheme 1). This could impact the outcome of a large range of asymmetric transformations that are mediated by chiral Brønsted-acids.

For this reason, we have now performed a detailed mechanistic study, trying to shed light on these effects. We investigated the influence of the catalyst structure and loading, using catenated, macrocyclic and acyclic phosphoric acids as catalysts (catalysts **1**/**2**/**3**, Scheme 2). This enabled us to understand how the competing catalytic pathways impact the catalytic reaction in terms of reaction rates and stereoselectivities, thus demonstrating the importance of acid–acid interactions in Brønsted-acid organocatalysis.

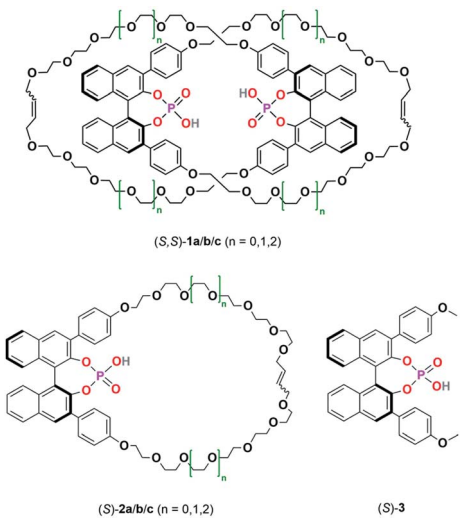


Scheme 2 Catenated catalysts (*S*,*S*)-**1a**/**b**/**c**, macrocyclic catalysts (*S*)-**2a**/**b**/**c** and acyclic catalyst (*S*)-**3** used in this study.

# Results and discussion

## General approach

The reactivity and stereoselectivity of the three different catalysts were investigated using the reduction of 2-phenylquinoline **4** with dihydropyridine **7** (Hantzsch-ester) to give tetrahydroquinoline **6** and pyridine **8** (Table 1). The reaction was carried out in toluene at 25 °C, as established previously.[17]

Time-resolved data were obtained by NMR-spectroscopy. Rate constants were determined by both nonlinear fitting[19] and linear fitting of the conversion plots, which gave almost identical results (ESI Tables S4–S7‡ and chapter 9). We also performed reaction progress kinetic analysis (RPKA) based on different and same excess measurements.[20] Mechanistic information was obtained by variable time normalization analysis (VTNA, see the ESI‡ chapter 4.4).[21,22]

## Influence of the catenane ring sizes

As a starting point, we employed catenanes **1a**/**b**/**c** with varying ring-sizes, assuming that the ring-size will influence the (mechano)intramolecular acid–acid interactions, thus affecting reaction rates and stereoselectivities. In addition to the previously reported hexaethyleneglycol-based species **1b**/**2b**,[16] we generated the smaller, pentaethyleneglycol-based systems **1a**/**2a** and the larger, heptaethyleneglycol-based systems **1c**/**2c** (ESI‡ chapter 2). Interestingly, there is a clear increase in yields of both catenanes and macrocycles with increasing ring size (5%/7%/10% for **1a**/**b**/**c** and 8%/11%/15% for **2a**/**b**/**c**),[23] suggesting that the longer linkers have a sufficient length for the intramolecular ring-closing metathesis, while the shorter linkers lead to increased formation of oligomeric byproducts.

In catalysis, the catenanes **1a**/**b**/**c** show drastically enhanced stereoselectivities in comparison to the macrocycles **2a**/**b**/**c** (as earlier reported for the **1b**/**2b** pair).[17] However, the was no impact of the ring-sizes on stereoinduction: Enantiomeric excesses were in the range of 81–84% in favor of the (*R*)-product for catenanes (*S*,*S*)-**1a**/**b**/**c**, while the macrocycles (*S*)-**2a**/**b**/**c** consistently favored the (*S*)-product with 12–17% ee. However,

Table 1 Results of the transfer-hydrogenation of 2-phenylquinoline with catalysts **1a**/**b**/**c** and **2a**/**b**/**c**

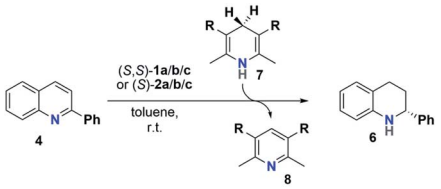


| Catalyst[a] | ee[b] [%] | $v_0$ [$10^{-7}$ M $s^{-1}$] | Catalyst[a] | ee[b] [%] |
|---|---|---|---|---|
| (*S*,*S*)-**1a** | 81 | 3.7 | (*S*)-**2a** | −17 |
| (*S*,*S*)-**1b** | 84 | 3.1 | (*S*)-**2b** | −12 |
| (*S*,*S*)-**1c** | 82 | 2.0 | (*S*)-**2c** | −17 |

[a] 2.5 mol% catalyst, 5 mM quinoline. [b] Determined by chiral HPLC. Values given for the excess of (*R*)-**6**.


This journal is © The Royal Society of Chemistry 2020

Open Access Article. Published on 07 2020. Downloaded on 07/01/2026 18:02:33.
This article is licensed under a Creative Commons Attribution-NonCommercial 3.0 Unported Licence.

the reaction rates of **1a**/**b**/**c** clearly depend on the ring-size, with the smaller catenanes showing higher rates ($v_0 = 3.7 \times 10^{-7}$/3.1 $\times$ $10^{-7}$/2.0 $\times$ $10^{-7}$ M $s^{-1}$ for **1a**/**b**/**c** at 10% catalyst loading). This suggests that the geometry of the stereodetermining transition-states is not influenced by the ring-sizes, but the reaction rates are decreased. This might be due to intramolecular hydrogen bonding of the P(O)OH-unit to the ethylene glycol units (as found in our earlier DFT work[17]), which might be more prevalent in the larger systems.

### First reduction step: kinetic analysis

The mechanism for the phosphoric acid catalyzed transfer-hydrogenation of quinolines involves two steps (Scheme 3): first, quinoline **4** is reduced to the corresponding 1,4-dihydroquinoline **5**, followed by reduction to the chiral 1,2,3,4-tetrahydroquinoline **6**. Both steps involve activation of the substrate by protonation, followed by Hantzsch-ester coordination, hydride-transfer and product-dissociation. Like other phosphoric acid-catalyzed reactions, the stereoselectivity of such transfer-hydrogenation strongly depends on the nature of the phosphoric acid, with bulky 3,3′-substituents allowing for high stereoselectivities.[9] Thus, excellent selectivities were achieved even at low catalyst loadings for 2-arylquinolines[4a] or benzoxazines[4b] using a phosphoric acid with phenanthryl-groups in the 3,3′-positions.

This catalytic mechanism[3,24] closely resembles the related transfer-hydrogenation of imines.[25] Our recent DFT results support this mechanism and suggest that the rate-limiting transition state occurs in the first reduction of **4** to **5**, namely in the protonation of the 1,4-dihydroquinoline-species. In comparison, the subsequent stereoselective second reduction towards **6** has a lower barrier. Moreover, our DFT-results suggest an additional mechanistic pathway involving two phosphoric acids, which we assume in the case of the catenane-catalysts **1**.[17]

However, to the best of our knowledge, an experimental elucidation of these mechanisms has not been reported. To probe the suggested mechanism, we firstly determined the reaction orders for substrates **4** and **7** (reaction orders $m$, $n$) and the role of product inhibition. Secondly, the order of the catalyst (reaction order $p$) was determined for the catalysts **1c**/**2c**/**3**

$$v = -\frac{d[Q]}{dt} = k_{Obs}[Q]^m[HE]^n = k[Cat]^p[Q]^m[HE]^n \qquad (1)$$

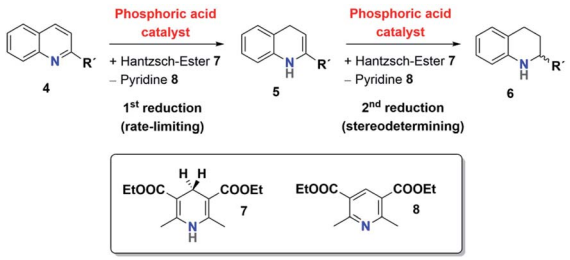


Scheme 3 Two-step transfer-hydrogenation of quinolines **4** to tetrahydroquinolines **6**.

The first analysis of the time-resolved NMR-data (ESI Fig. S2/S3‡) shows that the reduction of **4** to **6** occurs selectively with no side products. The intermediate 1,4-dihydroquinoline was not observed in any of our experiments, mainly due to its high free energy (low concentration) as suggested by our recent DFT-calculations.[17] Since the reduction of **4** to **5** is rate-limiting, the reaction orders $p$, $m$, $n$ describe the first reduction step from **4** to **5**.

### Substrate orders and product inhibition

For the catenated catalyst **1c**, rate measurements at different concentrations of quinoline **4** and Hantzsch-ester **7** indicated linear dependence of the reaction rate on the substrate concentrations. In the resulting ln $v_0$/ln[substrate] plots (Fig. 1a and b), we could determine reaction orders of 0.8 (for **4**) and 0.7 (for **7**), respectively. This is in good agreement with the VTNA-plots (Fig. 1c and d, see Fig. S7‡ for other values of $m$/$n$), which show excellent overlap of all curves for substrate orders of 1 for both the quinoline and the Hantzsch-ester.

Accordingly, the substrate orders for the macrocyclic catalyst and acyclic catalysts **2c**/**3** were determined based on VTNA only. It was found that both substrates have a reaction order of close to 1 for both catalysts (ESI Fig. S11/S15‡). Thus, there is no difference with regard to the substrate orders for the different catalysts **1c**/**2c**/**3**. In addition, we performed same excess experiments in order to investigate potential catalyst deactivation or product inhibition (ESI Fig. S10/S14/S19‡). In all cases, we observed only minor differences so that there seems to be neither catalyst deactivation nor product inhibition for all three catalysts **1c**/**2c**/**3**.

### Catalyst orders and aggregation

The reaction orders of the catalysts were determined in a series of experiments with different concentrations of catalysts **1c**/**2c**/**3**. For the catenated and macrocyclic catalysts **1c**/**2c**, the $v_0$ *vs.*

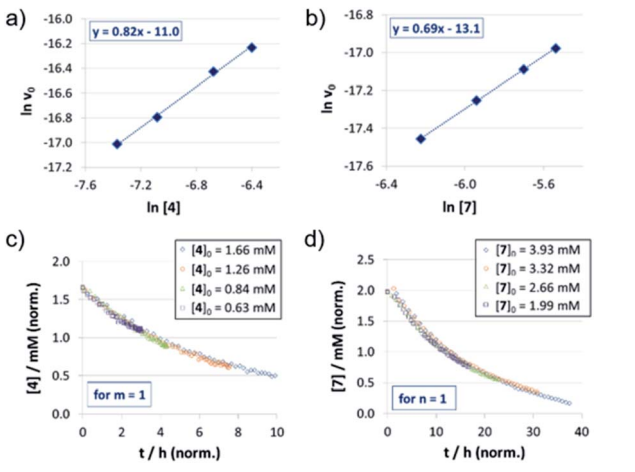


Fig. 1 Substrate order determination by different excess experiments for quinoline **4**(a, c) and Hantzsch-ester **7** (b, d) in the case of catenane **1c**: ln $v_0$/ln[substrate] plots ($v_0$ in $M^{-1}$ $s^{-1}$, substrate concentrations in M) (a, b) and VTNA-plots (c, d).

Open Access Article. Published on 07 2020. Downloaded on 07/01/2026 18:02:33.
This article is licensed under a Creative Commons Attribution-NonCommercial 3.0 Unported Licence.

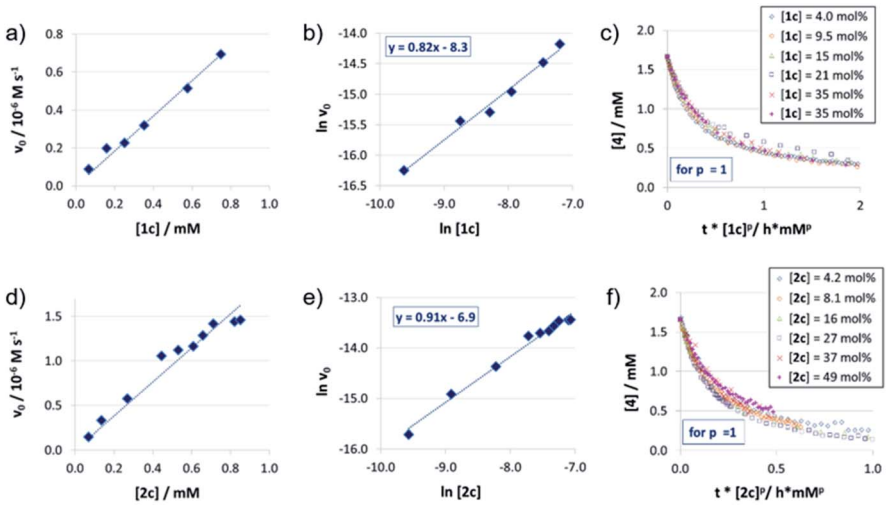


Fig. 2 Catalyst order determination for catalysts **1c** (a, b, c) and **2c** (d, e, f): initial rates (all at 1.66 mM quinoline **4** and 3.93 mM Hantzsch-ester **7**) (a, d), ln $v_0$/ln[catalyst] plots ($v_0$ in $M^{-1}$ $s^{-1}$, catalyst concentrations in M) (b, d) and VTNA-plots (selected catalyst concentrations only) (c, f).

[catalyst] plots (Fig. 2a and d) show a linear increase in rate upon increasing the catalyst loading in a range of 5–50 mol%. Thus, we could determine the order of catalysts based on respective double logarithmic plots (Fig. 2b and e), resulting in catalyst orders of 0.82 (for the bifunctional catenane **1c**) and 0.91 (for the monofunctional macrocycle **2c**). Once again, the first order dependence is also found by VTNA, which shows good overlap for $p = 1$ in both cases (Fig. 2c and f, for other values of $p$ see the ESI Fig. S9/S13‡).

For the macrocyclic catalyst **2c**, the linear rate *vs.* loading behaviour and the catalyst order of $p = 1$ shows that this system reacts *via* the monomeric pathway, independent of the catalyst concentration. As for the catenane **1c**, the linear rate *vs.* loading relationship also indicates that this system consistently follows one catalytic mechanism only, although the catalyst order ($p = 1$) alone does not allow us to conclude if the monomeric or dimeric catalyst pathway is dominating. However, the initial rate of the catenated catalyst **1c** is significantly lower than that of the macrocyclic catalyst **2c** (*e.g.* $v_0 = 0.88/1.5 \times 10^{-7}$ M $s^{-1}$ for **1c**/**2c** at 0.07 mM catalyst loading), despite the fact that the catenated catalyst features two phosphoric acid units. This is in line with the DFT-calculated lower rate for a dimeric catalyst pathway. Based on these combined data, we assume that the dimeric catalysis pathway is dominating for the catenated catalyst **1c** in the first, rate-determining reaction step.

In contrast to catalysts **1c**/**2c**, the acyclic phosphoric acid **3** shows a nonlinear behavior: in the $v_0$ *vs.* [**3**] plot (Fig. 3a); increase of catalyst loading leads to a much stronger rate increase at lower loadings than it does at higher loadings. Looking at the normalized initial rates $v_0$/[**3**] (Fig. 3b), we found that the normalized rate decreases initially, before it reaches a plateau at higher loadings. In order to see if the nonlinear behavior of the rate is due to a change in the catalyst order, we performed VTNA. While we find an order of $p = 1.25$ at low catalyst loadings, the VTNA shows a larger order of $p = 1.75$ at high catalyst loadings (Fig. 3c and d, for other values of $p$ see the ESI Fig. S17/S18‡). Thus, we believe that the nonlinear behavior of **3** can be interpreted based on competing reaction mechanisms: At low catalyst concentrations, the monomeric pathway is dominating, although the dimeric pathway still contributes. *Vice versa*, the dimeric pathway, which involves two phosphoric acids in the rate-determining transition state, dominates at higher catalyst loadings.

In order to relate these orders of catalysts to the overall observed reaction rates (as shown in Fig. 3a), it must be noted that the rate not only depends on the relative concentrations of the competing rate-determining intermediates (involving one or

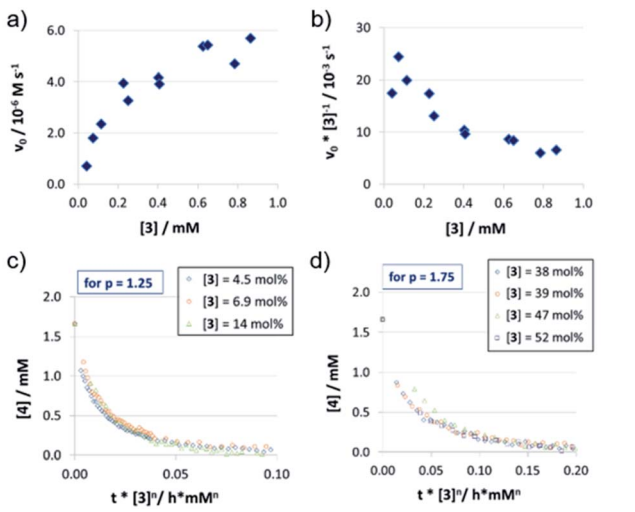


Fig. 3 Catalyst order determination for catalyst **3**: initial rates (a) and normalized initial rates (b) (all at 1.66 mM quinoline **4** and 3.93 mM Hantzsch-ester **7**) and VTNA-plots at low (c) and high (d) catalyst concentrations (selected catalyst concentrations only).

 This journal is © The Royal Society of Chemistry 2020

Open Access Article. Published on 07 2020. Downloaded on 07/01/2026 18:02:33.
This article is licensed under a Creative Commons Attribution-NonCommercial 3.0 Unported Licence.

two catalyst molecules), but also on the corresponding reaction rates of the monomeric and the dimeric pathways.

### Normalized reaction rates and influence of dimerization

The normalized initial rates $v_{norm} = v_0/[Cat]$ (Table 2; also see the ESI Fig. S20‡) are almost constant for different catalyst loadings in the case of **1c**/**2c** ($v_{norm}$ (**1c**) = $1.04 \times 10^{-3}$ $s^{-1}$ and $v_{norm}$ (**2c**) = $2.06 \times 10^{-3}$ $s^{-1}$), as would be expected based on the linear rate *vs.* loading relationship. In the nonlinear case of catalyst **3**, the maximum initial rate, equivalent to the rate constant for the purely monomeric pathway, can be obtained as the *y*-intercept in a linear extrapolation for low catalyst loadings ($v_{max} = v_{norm}(\mathbf{3}_{mono}) = 22.7 \times 10^{-3}$ $s^{-1}$). In turn, the maximum rate for the dimeric pathway can be estimated from the plateau for high catalyst loadings ($v_{norm}(\mathbf{3}_{Di}) = <6.29 \times 10^{-3}$ $s^{-1}$).

This shows that there is a smaller difference in normalized initial rates for the macrocycle/catenane pair ($v_{norm}$(**2c**)/$v_{norm}$(**1c**) = 1.98) than for the monomeric/dimeric pathway for catalyst **3** ($v_{norm}(\mathbf{3}_{mono})/v_{norm}(\mathbf{3}_{Di})$ = 3.61). The difference between the macrocyclic and acyclic catalysts is even more pronounced ($v_{norm}(\mathbf{3}_{Di})/v_{norm}$(**1c**) = 6.05 and $v_{norm}(\mathbf{3}_{mono})/v_{norm}$(**2c**) = 11.0), showing that the ethylene-glycol chains significantly reduce the reaction rate (as already seen for the different sized catenanes **1a**/**b**/**c**).

### Detailed analysis of the acyclic phosphoric acid 3

As detailed above, the nonlinear rate-behavior for the acyclic catalyst **3** can be attributed to both concentration effects and a change in the rate constant. At higher concentrations, a smaller number of active species is present (since two molecules of **3** are needed in the dimeric pathway), together with a smaller rate constant for this pathway ($v_{norm}(\mathbf{3}_{mono})/v_{norm}(\mathbf{3}_{Di})$ = 3.61, *vide supra*). Thus, the total rate data (Fig. 3) were analyzed in order to determine the mole fractions of catalysts that act *via* the monomeric and the dimeric pathway, respectively (ESI‡ chapter 5). The resulting speciation plot[26] (Fig. 4a) reveals that under the employed conditions (1.66 mM quinoline, 3.93 mM Hantzsch-ester, toluene solvent), the crossing point of both curves lies at *ca.* 0.25 mM catalyst (15 mol%). However, taking into account the lower relative rate for the dimeric pathway, the impact of catalyst-dimerization on the total rate is less significant (Fig. 4b), and only above 0.4 mM, the contribution of the dimeric pathway exceeds that of the monomeric pathway.

Table 2 Normalized initial rates for **1c**/**2c**/**3**

| Catalyst | $v_0/[Cat]$ [$10^{-3}$ $s^{-1}$] |
|---|---|
| **1c** | 1.04[a] |
| **2c** | 2.06[a] |
| $\mathbf{3}_{Di}$ (>0.6 mM) | <6.29[b] |
| $\mathbf{3}_{mono}$ (<0.25 mM) | 22.7[c] |

[a] Mean value for all catalyst concentrations. [b] Mean value for catalyst concentrations >0.6 mM. [c] Determined as the *y*-intercept in the $v_0$/[Cat] plot for loading <0.25 mM.

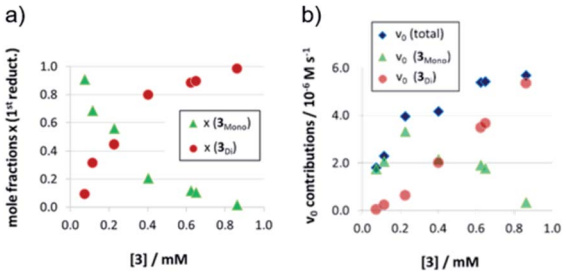


Fig. 4 Mole fractions (a) and $v_0$ contributions (b) for the monomeric and dimeric pathway for different concentrations of catalyst **3** for the first reduction step [$x(\mathbf{3}_{mono})$: mole fraction of monomeric catalyst, $x(\mathbf{3}_{Di})$: mole fraction of phosphoric acid **3** bound in a dimeric catalyst].

### Second reduction step: influence of aggregation on stereoselectivity

The rate analysis does not give any insight into the second, stereodetermining reduction step. Thus, we investigated the influence of the overall concentration and catalyst loading on the enantiomeric excess of the tetrahydroquinoline product **6** since this gives direct information about the second reduction.

Firstly, we found that at higher overall concentrations (5.0 mM instead of 1.66 mM quinoline) but identical absolute catalyst concentrations, stereoselectivities shift towards (*R*)-**6** (*e.g.* +20%/-22% ee at 25 mM catalyst, meaning 1.5/0.5 mol% loading at 1.66/5.0 mM quinoline concentration, Fig. S21b‡). However, for identical relative catalyst loadings, we find almost identical stereoselectivities (*e.g.* +72%/+71% ee at 50 mol%, meaning 0.83/2.5 mM catalyst concentration at 1.66/5.0 mM quinoline concentration, Fig. S21c‡). Thus, the stereoselectivity depends mostly on the substrate/catalyst ratio, which would be in line with competing monomeric and dimeric catalyst pathways: high substrate concentrations favour the formation of catalyst·dihydroquinoline·Hantzsch-ester complexes at the expense of higher-order catalyst·catalyst·dihydroquinoline·Hantzsch-ester complexes, thus shifting the reaction towards the less stereoselective, monomeric pathway.

Secondly, we checked whether there is a dependence of stereoselectivity on conversion since changing concentrations of substrates **4**/**7** and products **6**/**8** might influence the distribution between monomeric and dimeric pathways based on different association constants. However, no change in stereoselectivity was found between 15 and 95% conversion at 1 mol% catalyst loading (ESI Table S11 and Fig. S25‡).

Thirdly, we investigated the influence of catalyst loading over a broad concentration range (0.0017 mM to 0.83 mM catalyst concentration, meaning 0.1 to 50 mol% at 1.66 mM quinoline). We observed that there is a drastic change in enantioselectivity (Fig. 5): At low catalyst concentrations, the (*S*)-product enantiomer is favored (−30% ee), while at high catalyst concentrations the selectivity reaches up to 72% ee in favor of the (*R*)-isomer.

This means that the monomeric catalyst and the dimeric pathway not only have different, but actually inverted

Open Access Article. Published on 07 2020. Downloaded on 07/01/2026 18:02:33.
This article is licensed under a Creative Commons Attribution-NonCommercial 3.0 Unported Licence.

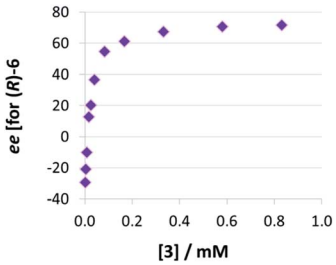


Fig. 5 Influence of catalysts loading on enantioselectivities for catalyst **3** (given as enantiomeric excess for (*R*)-**6**).

stereoselectivities. This reflects the enantioselectivities of the macrocyclic and catenated catalysts **2c**/**1c** (−17% ee/+84% ee), which underpins their predominant reactivity *via* monomeric (for **2c**) and dimeric (for **1c**) catalytic pathways. A control experiment using 1 mol% phosphoric acid **3** plus 49 mol% benzoic acid (+10% ee, *cf.* +13% ee for 1 mol% **3** only) showed that the dimeric pathway requires high concentrations of phosphoric acid and the same effect cannot be easily achieved when using carboxylic acids as assisting Brønsted-acids (ESI Table S1‡).

The strong curvature of the ee *vs.* [**3**] curve suggests that the dimeric (more stereoselective) pathway has a stronger contribution in the second reduction step than in the first reduction step. This is in line with our previous DFT-results, which indicate that for the stereodetermining step, the dimeric pathway actually possesses a lower barrier than its monomeric counterpart (6.8 kcal mol$^{-1}$ *vs.* 8.5 kcal mol$^{-1}$).[17] To generate the corresponding speciation plot, we estimated the relative rates of the monomeric and dimeric pathway based on the DFT-data ($k(\mathbf{3}_{Di})/k(\mathbf{3}_{mono}) = 17.7$, according to $\Delta E_A = 1.7$ kcal mol$^{-1}$),[17] since these data are not directly available experimentally. The resulting plot shows a different distribution of monomeric and dimeric pathways in comparison to the first reduction step (Fig. 6a). The mole fraction of the catalyst acting *via* the dimeric pathway is lower, and the crossing of both curves is observed at *ca.* 0.5 mM catalyst loading (30 mol%). However, the impact of the dimeric pathway on the second reduction (and thus on the stereoselectivity) is significantly enhanced by its higher relative rate (Fig. 6b). Only below a catalyst concentration of 0.012 mM (0.7 mol%), the enantioselectivity is dominated by the monomeric pathway, leading to overall preference for the (*S*)-product. At 0.17 mM (10 mol%) loading, the stereoselectivity already reaches 61% ee for the (*R*)-isomer, which is close to the highest stereoselectivity of 72% observed at 0.83 mM (50 mol%) loading. This demonstrates the relative importance of the dimeric pathway in terms of stereoselectivity, even at low catalyst loadings.

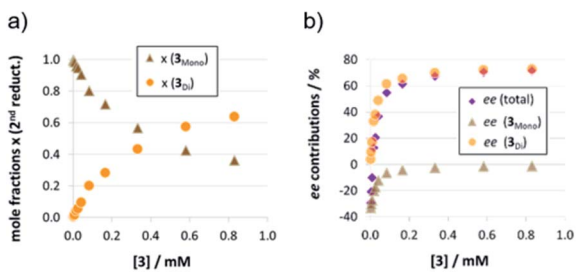


Fig. 6 Mole fractions (a) and ee contributions (b) for the monomeric and dimeric pathway for different concentrations of catalyst **3** for the second reduction step.

## NMR-spectroscopic investigation of catalyst dimerization

**Model systems and experimental conditions.** Next, detailed NMR-spectroscopic studies were performed to elucidate the structural space including the dimeric reaction pathway for acyclic catalyst **3**. Temperatures between 180 and 200 K were used to sufficiently slow down exchange processes and to detect separated hydrogen bonded protons (ESI Fig. S26‡). Since in toluene **3** was nearly insoluble at these temperatures, $CD_2Cl_2$ was used, which provided sufficient solubility and signal dispersion (for spectra and solvents see the ESI Fig. S27‡).[27] In addition, DFT-calculations at the TPSS-D3/def2-QZVP + COSMO-RS//TPSS-D3/def2-SVP + DCOSMO-RS level of theory[28] showed that analogous species should be present in $CD_2Cl_2$ and toluene (ESI‡ chapter 7). Experimentally, we verified that in dichloromethane there is also a strong influence of catalyst loading on enantioselectivities. As expected by DFT, the absolute stereoselectivities in dichloromethane are lower (−33% to −6% ee for 1–50 mol% catalyst loading, ESI Fig. S28‡), nevertheless showing that competing monomeric and dimeric pathways are also operating in dichloromethane.

For structural NMR-investigations, quinolines **4b–d** (Fig. 7A) were selected as model substrates as they possess suitable probes for $^1$H and $^{19}$F NMR spectroscopy. Furthermore, they modulate the basicity of the quinoline and thus allow for alteration of the hydrogen bond strength. Samples with a 1 : 1 or 2 : 1 stoichiometry of **3** : **4b–d** at NMR suitable

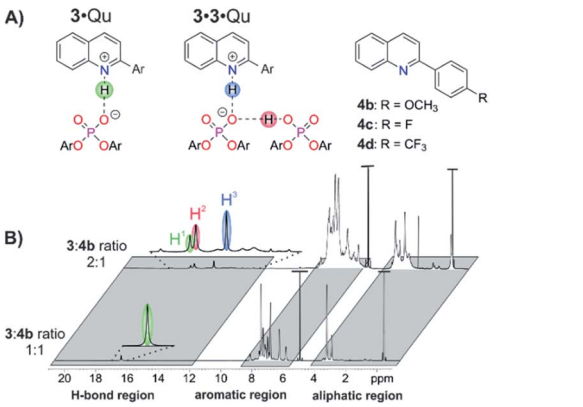


Fig. 7 (A) Schematic structures of the **3**·Qu and **3**·**3**·Qu complexes and substituents of quinolines **4b–d**. (B) Spectral resolution of the $^1$H spectra of complexes of **3** and **4b** at a 1 : 1 or 2 : 1 stoichiometry at 200 K and 600 MHz in $CD_2Cl_2$. In the 1 : 1 system, only one H-bond is detected, presumably of the **3**·**4b** complex. For the 2 : 1 system, three major H-bonds are observed at 16.76 (H1), 16.51 (H2) and 15.27 ppm (H3), most likely of the **3**·**4b** (H1) and **3**·**3**·**4b** (H2 and H3) complex.


This journal is © The Royal Society of Chemistry 2020

Open Access Article. Published on 07 2020. Downloaded on 07/01/2026 18:02:33.
This article is licensed under a Creative Commons Attribution-NonCommercial 3.0 Unported Licence.

concentrations (10–50 mM of **3**) were employed to study the structures of the complex **3**·Qu or the complex **3**·**3**·Qu, respectively.

**1 : 1 stoichiometries (3·Qu complexes).** To shed light on the structures involved in the monomeric catalysis pathway, samples of **3** and **4b–d** with a 1 : 1 stoichiometry were investigated. For **4b**, only one hydrogen bond proton signal was detected at 16.83 ppm (Fig. 7B), which is a typical chemical shift for protons in strong hydrogen bonds and is similar to the hydrogen bond signals in CPA·imine complexes.[13,29] The detection of magnetization transfer between the H-bond proton and both quinoline and CPA further corroborated the assignment of this hydrogen bond signal (ESI Fig. S30‡). The presence of the **3**·**4b** complex was further validated by diffusion ordered spectroscopy (DOSY) measurements. Similar hydrodynamic radii for **3** (9.11 ± 0.17 Å) and **4b** (7.2 ± 1.62 Å) revealed the dominant presence of the complex and are in the same order as the radii of CPA·imine complexes.[15] Using different homo- and heteronuclear 2D spectra, chemical shift assignment of **3**·**4b** (ESI Fig. S29‡) as well as in-depth NOE analysis could be accomplished (ESI Fig. S32‡). Two different conformations with a ≈180° rotated orientation of the quinolines were identified, which are in a fast exchange on the NMR time scale[14,15,30] (ESI Fig. S32‡ for a more detailed description of the structures and exchange pathway).[15] One of the conformations validated the previously computed structure of the **3**·Qu complex.[17]

Similar $^1$H spectra were obtained for quinolines **4c** and **4d**. Decreasing the basicity of the quinoline resulted in low field shifted proton signals (**4b**: 16.83 ppm, **4c**: 17.42 ppm, **4d**: 18.08 ppm; ESI Fig. S31‡), which corresponds to an increase in hydrogen bond strength.[31] Thus, similar to CPA·imine complexes,[13,29b] CPA·Qu complexes are present as hydrogen bond assisted ion pairs anchored by a strong, charge assisted hydrogen bond.[13,29b] At 1 : 1 ratios, higher aggregates, such as **3**·**3**·Qu complexes are below the NMR-detection limit. In summary, monomeric **3**·Qu complexes are analogous to the previously investigated CPA·imine systems[13–15,29b,30] and are at least for the monomeric pathway a representative of catalyst·substrate complexes in CPA catalyzed transformations.

**2 : 1 stoichiometries (3·3·Qu complexes).** In order to populate and characterize the **3**·**3**·Qu complex (Fig. 7A), samples of **3** to **4b–d** with a 2 : 1 stoichiometry were investigated. For quinoline **4b**, three dominant hydrogen bonded protons with a ratio of $H^1 : H^2 : H^3 \approx 1 : 2.4 : 2.4$ were observed (Fig. 7B).[32] Proton $H^1$ corresponds to the **3**·**4b** complex as it has a nearly identical chemical shift as the H-bond proton in the respective sample with a 1 : 1 stoichiometry ($\Delta\delta(^1H) = 0.07$ ppm). Protons $H^2$ and $H^3$ have similar integrals, which fits the expected hydrogen bonding situation for the **3**·**3**·**4b** complex. Protons $H^1$ and $H^3$ showed exchange signals in the NOE spectrum (ESI Fig. S33‡). In addition, both protons show similar low field shifts with quinolines **4c** and **4d**, *i.e.* a similar modulation of the H-bond strength (ESI Fig. S31‡).

Thus, proton $H^3$ is assigned to the $PO^-\cdots H\cdot N^+$ hydrogen bond (Fig. 7B, highlighted in blue) and proton $H^2$ to the $PO^-\cdots H\cdot OP$ hydrogen bond (Fig. 7B, highlighted in red) of the **3**·**3**·**4b** complex. The significant high field shift of proton $H^3$ compared to proton $H^1$ reveals a weaker $PO^-\cdots H\cdot N^+$ hydrogen bond, *i.e.* a stronger proton transfer on the quinoline in the **3**·**3**·**4b** complex compared to the **3**·**4b** complex.[31] This weakening is often found in bifurcated hydrogen bonds[29a] and can be rationalized by the compensation of an increasing negative partial charge on the phosphate by the additional $PO^-\cdots H\cdot OP$ hydrogen bond enabled by the second CPA.

For CPA·imine systems, a correlation between hydrogen bond strength and reactivity has been observed previously, giving lower reactivities for weaker hydrogen bonds.[13] This trend is also reflected for the monomeric and dimeric reaction pathways in the investigated quinoline systems, as the dimeric reaction pathway featuring a weaker $PO^-\cdots H\cdot N^+$ hydrogen bond shows lower reaction rates than the monomeric pathway (Fig. 8).

Moreover, additional hydrogen bond signals were observed in the $^1$H spectrum at a 2 : 1 stoichiometry, which are less populated and/or have severe line broadening (Fig. 7b, magnified H-bond region). EXSY signals in the NOESY spectrum revealed that these signals are in chemical exchange with the $PO^-\cdots H\cdot N^+$ or $PO^-\cdots H\cdot OP$ hydrogen bond protons of the **3**·**4b** and **3**·**3**·**4b** structures, thus suggesting the presence of different/higher aggregates of **3** and **4b**. Additional detailed NMR-structural analysis of the **3**·**3**·**4b** complex could not be achieved due to strong line broadening and signal overlaps (see the aromatic region in Fig. 7b).

Similar $^1$H spectra were obtained for quinolines **4c** and **4d** (ESI Fig. S31‡). Measurements at lower temperatures were not fruitful due to the poor solubility of **3** in the required freonic mixtures[27] ($CDCl_2F$ and $CDClF_2$). However, the spectra at 300 K were significantly simplified and better resolved, as the different species (free **3** and Qu, **3**·Qu, **3**·**3**·Qu and potential higher aggregates) are in fast exchange on the NMR time scale. DOSY measurements were performed at 1 : 1 and 2 : 1 stoichiometries to further confirm the postulated presence of **3**·**3**·**4b** in the 2 : 1 samples (ESI Table S13‡). Due to the chemical exchange of the different species, the measured diffusion coefficients and derived hydrodynamic radii are an average of the values of the different species, weighted by their respective population and lifetime.[33] Similar hydrodynamic radii were derived for the quinoline and the CPA, demonstrating that also at 300 K the catalyst–quinoline complexes are the dominant species (ESI Table S14‡). When comparing the derived hydrodynamic radii for the 1 : 1 and 2 : 1 stoichiometries, a size increase of ≈2.2 and 3.2 Å was observed for the quinolines **4b** and **4c** in the 2 : 1 samples, which is in agreement with the previously reported offset for CPA·imine complexes and their dimers (≈3 Å).[15] The increased radii clearly show that higher aggregates, such as the **3**·**3**·Qu complex, are populated when employing a 2 : 1 ratio of catalyst and quinoline.

## Overall mechanistic picture for catalyst 3

In summary, our combined kinetic, stereoselectivity, DFT and NMR analysis of the transfer-hydrogenation of quinolines with the acyclic catalyst **3** has revealed the following key findings (also see Fig. 8):

Open Access Article. Published on 07 2020. Downloaded on 07/01/2026 18:02:33.
This article is licensed under a Creative Commons Attribution-NonCommercial 3.0 Unported Licence.

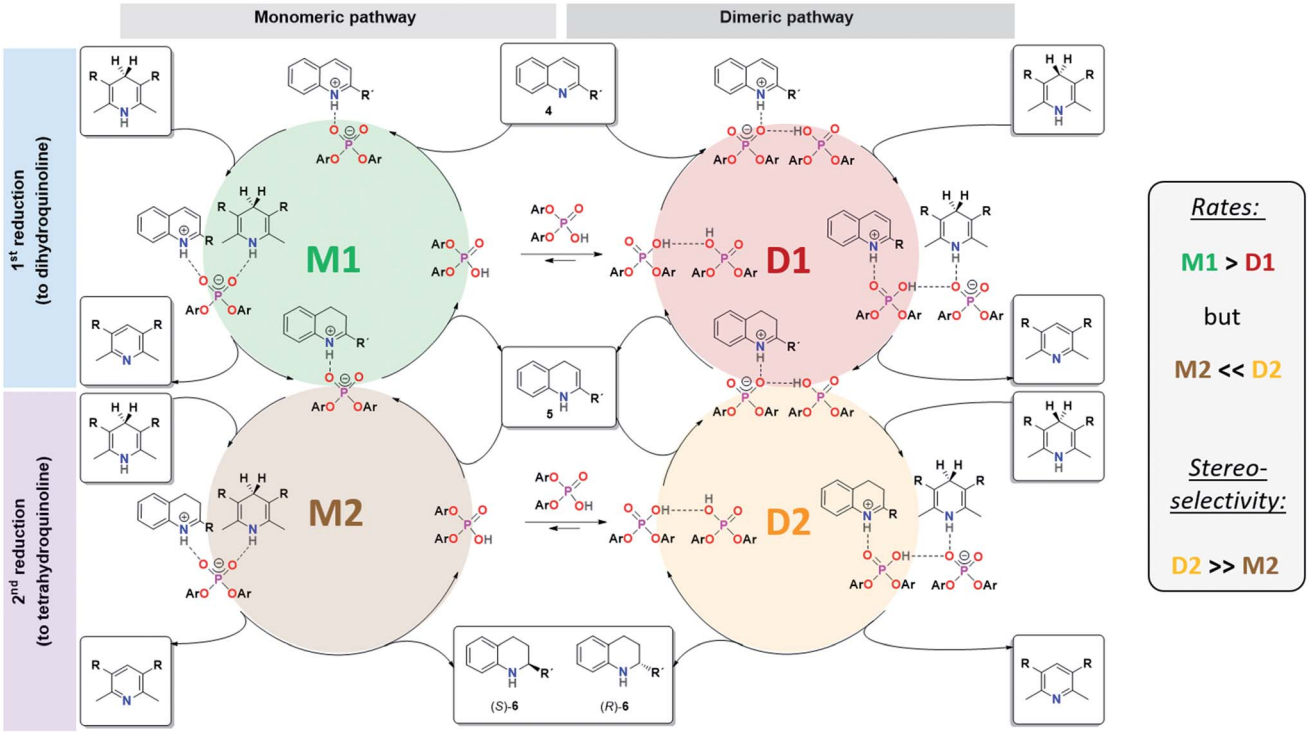


Fig. 8 Revised mechanistic picture for the transfer-hydrogenation of quinolines catalysted by chiral phosphoric acids.

- The catalytic reaction using catalyst **3** involves competing monomeric and dimeric pathways, as found by analysis of the kinetics and stereoselectivity and by DFT.

- Both the **3**·Qu and **3**·**3**·Qu complexes, which are relevant for the monomeric and dimeric pathways, were directly observed by low-temperature NMR-spectroscopy.

- For the first reduction step (**4** to **5**), kinetics, H-bond analysis and DFT jointly show that the reduction occurs faster for the monomeric catalyst than for the dimeric one (cycles M1 and D1, Fig. 8). For this reason, the influence of the dimeric pathway on the reaction rate is less pronounced and the dimeric pathway only dominates above 0.25 mM/15 mol% catalyst.

- For the second stereoselective reduction step, the effect of the catalyst concentration on stereoselectivity shows that the monomeric and dimeric pathways not only have different but even inversed stereoselectivities. This reflects the selectivities of the macrocyclic and catenated catalysts **1c**/**2c**.

- As corroborated by DFT, the stereoselective second reduction (**5** to **6**) occurs faster for the dimeric pathway (cycles M2 and D2, Fig. 8). Thus, the impact of catalyst dimerization on the stereoselectivity is much more pronounced, with the dimeric pathway dominating even at catalyst loadings as low as 0.012 mM (0.7 mol%).

## Conclusion

In conclusion, we have elucidated the importance of acid–acid interactions in phosphoric-acid based organocatalysis, using the transfer-hydrogenation of quinolines as an example. Based on a detailed mechanistic analysis of the catenated, macrocyclic and acyclic phosphoric acids **1**/**2**/**3**, we established that the catalytic reactions in the case of the catenated and macrocyclic catalysts **1**/**2** are dominated by the dimeric and the monomeric pathway, respectively. In stark contrast, but consistent with our recent DFT-work, the acyclic phosphoric acid **3** shows a concentration-dependent change in the reaction mechanism, involving either one or two catalyst molecules in the rate- and stereodetermining intermediates. The formation of complexes involving two catalyst species and one quinoline molecule was directly proven by NMR-spectroscopy. While the influence of these intermolecular acid–acid interactions on reaction kinetics is moderate, the impact on stereoselectivity is very pronounced, even leading to opposite enantioselectivities for the monomeric (−30% ee) and dimeric catalysis pathways (+72% ee). Based on these findings, we elaborated a revised mechanism for the phosphoric acid catalyzed transfer-hydrogenation of quinolines.

In comparison to other phosphoric-acid catalyzed transfer hydrogenations, it becomes clear that acid–acid interactions may well be relevant in these cases as well.[4,34] While we find a significant effect on the dimeric pathway at concentrations as low as 0.012 mM, commonly employed catalyst concentrations in the literature are significantly higher (ranging from 1 mM [4,34a,g] to 2 mM,[34d–f] 8 mM [34c] or even 10 mM [34b]). Certainly, the extent of intermolecular acid–acid interactions will depend strongly on the catalyst structure and has been shown to be lower for bulky phosphoric acids such as TRIP.[35] In addition, other factors such as the substrate structures and the solvent may favour or disfavour the formation of higher aggregates. Nevertheless, dimeric catalysis pathways may be relevant, if not


This journal is © The Royal Society of Chemistry 2020

Open Access Article. Published on 07 2020. Downloaded on 07/01/2026 18:02:33.
This article is licensed under a Creative Commons Attribution-NonCommercial 3.0 Unported Licence.

dominating, in other phosphoric-acid catalyzed transformations as well. We are currently investigating the influence of acid–acid interactions for other catalyst structures and other catalytic reactions in our laboratory, since a better understanding of such supramolecular interactions may have a major impact for the future development of phosphoric-acid catalyzed asymmetric transformations.

## Conflicts of interest

There are no conflicts to declare.

## Acknowledgements

Funding by the Fonds der Chemischen Industrie (Liebig-Fellowship to J. N.) and the German Research Foundation (DFG, NI1273/2-1) is gratefully acknowledged. J. N. would like to thank Prof. Carsten Schmuck for his support. J. G. thanks the Fonds der Chemischen Industrie for funding (Kekulé-Fellowship). J. G., H. Z., R. M. G. and S. G. thank the German Research Foundation (SPP 1807/2 Dispersion) for funding.

## Notes and references

1 A. Berkessel and H. Gröger, *Asymmetric Organocatalysis - From Biomimetic Concepts to Applications in Asymmetric Synthesis*, Wiley-VCH, Weinheim, 2005.
2 List's proline-catalyzed aldol reactions (see ref. 3) use a 30–40 mM catalyst, while Rueping's phosphoric acid catalyzed hydrogenation of quinolines (see ref. 4*a*) uses a 1–5 mM catalyst.
3 B. List, R. A. Lerner and C. F. Barbas, *J. Am. Chem. Soc.*, 2000, **122**, 2395–2396.
4 (*a*) M. Rueping, A. P. Antonchick and T. Theissmann, *Angew. Chem., Int. Ed.*, 2006, **45**, 3683–3686; (*b*) M. Rueping, A. P. Antonchick and T. Theissmann, *Angew. Chem., Int. Ed.*, 2006, **45**, 6751–6755.
5 D. D. Ford, D. Lehnherr, C. R. Kennedy and E. N. Jacobsen, *J. Am. Chem. Soc.*, 2016, **138**, 7860–7863.
6 C. R. Kennedy, D. Lehnherr, N. S. Rajapaksa, D. D. Ford, Y. Park and E. N. Jacobsen, *J. Am. Chem. Soc.*, 2016, **138**, 13525–13528.
7 Y. Park, K. C. Harper, N. Kuhl, E. E. Kwan, R. Y. Liu and E. N. Jacobsen, *Science*, 2017, **355**, 162–166.
8 (*a*) S. H. Oh, H. S. Rho, J. W. Lee, J. E. Lee, S. H. Youk, J. Chin and C. E. Song, *Angew. Chem., Int. Ed.*, 2008, **47**, 7872–7875; (*b*) H. S. Rho, S. H. Oh, J. W. Lee, J. Y. Lee, J. Chin and C. E. Song, *Chem. Commun.*, 2008, 1208–1210; (*c*) H. B. Jang, H. S. Rho, J. S. Oh, E. H. Nam, S. E. Park, H. Y. Bae and C. E. Song, *Org. Biomol. Chem.*, 2010, **8**, 3918–3922; (*d*) G. Tárkányi, P. Király, T. Soós and S. Varga, *Chem.–Eur. J.*, 2012, **18**, 1918–1922; (*e*) R. Salvio, L. Massaro, A. Puglisi, L. Angelini, A. Antenucci, S. Placidi, F. Sciubba, L. Galantini and M. Bella, *Org. Biomol. Chem.*, 2018, **16**, 7041–7049.
9 (*a*) D. Parmar, E. Sugiono, S. Raja and M. Rueping, *Chem. Rev.*, 2014, **114**, 9047–9153; (*b*) D. Parmar, E. Sugiono, S. Raja and M. Rueping, *Chem. Rev.*, 2017, **117**, 10608–10620; (*c*) L. Schreyer, R. Properzi and B. List, *Angew. Chem., Int. Ed.*, 2019, **58**, 12761–12777.
10 N. Li, X.-H. Chen, S.-M. Zhou, S.-W. Luo, J. Song, L. Ren and L.-Z. Gong, *Angew. Chem., Int. Ed.*, 2010, **49**, 6378–6381.
11 C. Detering, P. M. Tolstoy, N. S. Golubev, G. S. Denisov and H.-H. Limbach, *Dokl. Phys. Chem.*, 2001, 353–356.
12 C. Malm, H. Kim, M. Wagner and J. Hunger, *Chem.–Eur. J.*, 2017, **23**, 10853–10860.
13 K. Rothermel, M. Melikian, J. Hioe, J. Greindl, J. Gramüller, M. Žabka, N. Sorgenfrei, T. Hausler, F. Morana and R. M. Gschwind, *Chem. Sci.*, 2019, **114**, 1929.
14 J. Greindl, J. Hioe, N. Sorgenfrei, F. Morana and R. M. Gschwind, *J. Am. Chem. Soc.*, 2016, **138**, 15965–15971.
15 M. Melikian, J. Gramüller, J. Hioe, J. Greindl and R. M. Gschwind, *Chem. Sci.*, 2019, **10**, 5226–5234.
16 R. Mitra, M. Thiele, F. Octa-Smolin, M. C. Letzel and J. Niemeyer, *Chem. Commun.*, 2016, **52**, 5977–5980.
17 R. Mitra, H. Zhu, S. Grimme and J. Niemeyer, *Angew. Chem., Int. Ed.*, 2017, **56**, 11456–11459.
18 For reviews on acid–acid interactions in organocatalysis see: (*a*) H. Yamamoto and K. Futatsugi, *Angew. Chem., Int. Ed.*, 2005, **44**, 1924–1942; (*b*) C. Min and D. Seidel, *Chem. Soc. Rev.*, 2017, **46**, 5889–5902; (*c*) R. Mitra and J. Niemeyer, *ChemCatChem*, 2018, **10**, 1221–1234.
19 C. L. Perrin, *J. Chem. Educ.*, 2017, **94**, 669–672.
20 (*a*) D. G. Blackmond, *Angew. Chem., Int. Ed.*, 2005, **44**, 4302–4320; (*b*) J. S. Mathew, M. Klussmann, H. Iwamura, F. Valera, A. Futran, E. A. C. Emanuelsson and D. G. Blackmond, *J. Org. Chem.*, 2006, **71**, 4711–4722.
21 (*a*) J. Burés, *Angew. Chem., Int. Ed.*, 2016, **55**, 16084–16087; (*b*) J. Burés, *Angew. Chem., Int. Ed.*, 2016, **55**, 2028–2031; (*c*) C. D.-T. Nielsen and J. Burés, *Chem. Sci.*, 2019, **10**, 348–353.
22 The translation of the concentration vs. time profiles into reaction rates adds additional inaccuracy in the data analysis. This is avoided by directly using concentration vs. time profiles in VTNA instead of using rate vs. time profiles in classical RPKA.
23 Yields for **1b**/**2b** are lower than reported earlier (14%/22%) [see ref. 16]. We attribute this to a different chromatography system that was used for this work.
24 (*a*) J. P. Reid and J. M. Goodman, *Org. Biomol. Chem.*, 2017, **15**, 6943–6947; (*b*) J. P. Reid and J. M. Goodman, *Chem.–Eur. J.*, 2017, **23**, 14248–14260; (*c*) J. P. Reid, L. Simón and J. M. Goodman, *Acc. Chem. Res.*, 2016, **49**, 1029–1041; (*d*) L. Simón and J. M. Goodman, *J. Am. Chem. Soc.*, 2008, **130**, 8741–8747; (*e*) Y. Shibata and M. Yamanaka, *J. Org. Chem.*, 2013, **78**, 3731–3736; (*f*) T. Marcelli, P. Hammar and F. Himo, *Chem.–Eur. J.*, 2008, **14**, 8562–8571.
25 J. Pastor, E. Rezabal, A. Voituriez, J.-F. Betzer, A. Marinetti and G. Frison, *J. Org. Chem.*, 2018, **83**, 2779–2787.
26 For the dimeric catalyst, the mole fraction represents the amount of catalyst that is bound in the dimeric catalyst (meaning that the molar amount of dimeric catalyst is half of the molar amount of phosphoric acid as expressed by the mole fraction).

Open Access Article. Published on 07 2020. Downloaded on 07/01/2026 18:02:33.
This article is licensed under a Creative Commons Attribution-NonCommercial 3.0 Unported Licence.

27 J. S. Siegel and F. A. L. Anet, *J. Org. Chem.*, 1988, **53**, 2629–2630.

28 (*a*) S. Grimme, C. Bannwarth and P. Shushkov, *J. Chem. Theory Comput.*, 2017, **13**, 1989–2009; (*b*) S. Grimme and C. Bannwarth, *J. Chem. Phys.*, 2016, **145**, 054103; (*c*) P. Shushkov and S. Grimme, unpublished; (*d*) TURBOMOLE V7.0 2015, a development of University of Karlsruhe and Forschungszentrum Karlsruhe GmbH, 1989–2007, TURBOMOLE GmbH, since 2007; available from http://www.turbomole.com; (*e*) J. M. Tao, J. P. Perdew, V. N. Staroverov and G. E. Scuseria, *Phys. Rev. Lett.*, 2003, **91**, 146401; (*f*) S. Grimme, J. Antony, S. Ehrlich and H. Krieg, *J. Chem. Phys.*, 2010, **132**, 154104; (*g*) S. Grimme and L. Goerigk, *J. Comput. Chem.*, 2011, **32**, 1456–1465; (*h*) A. Schäfer, H. Horn and R. Ahlrichs, *J. Chem. Phys.*, 1992, **97**, 2571; (*i*) F. Weigend, *Phys. Chem. Chem. Phys.*, 2006, **8**, 1057; (*j*) S. Sinnecker, A. Rajendran, A. Klamt, M. Diedenhofen and F. Neese, *J. Phys. Chem. A*, 2006, **110**, 2235–2245; (*k*) A. Klamt and G. Schüürmann, *J. Chem. Soc., Perkin Trans. 1*, 1993, **2**, 799–805; (*l*) K. Eichkorn, F. Weigend, O. Treutler and R. Ahlrichs, *Theor. Chem. Acc.*, 1997, **97**, 119–124; (*m*) P. Deglmann, K. May, F. Furche and R. Ahlrichs, *Chem. Phys. Lett.*, 2004, **384**, 103–107; (*n*) S. Grimme, *Chem.–Eur. J.*, 2012, **18**, 9955–9964; (*o*) F. Weigend, F. Furche and R. Ahlrichs, *J. Chem. Phys.*, 2003, **119**, 12753; (*p*) F. Eckert and A. Klamt, *COSMOtherm, Version C3.0, Release 14.01*, COSMOlogic GmbH & Co. KG, Leverkusen, Germany, 2013; (*q*) A. Klamt, *J. Phys. Chem.*, 1995, **99**, 2224–2235; (*r*) F. Eckert and A. Klamt, *AIChE J.*, 2002, **48**, 369–385.

29 (*a*) T. Steiner, *Angew. Chem., Int. Ed.*, 2002, **41**, 48–76; (*b*) N. Sorgenfrei, J. Hioe, J. Greindl, K. Rothermel, F. Morana, N. Lokesh and R. M. Gschwind, *J. Am. Chem. Soc.*, 2016, **138**, 16345–16354.

30 N. Lokesh, J. Hioe, J. Gramüller and R. M. Gschwind, *J. Am. Chem. Soc.*, 2019, **141**, 16398–16407.

31 S. Sharif, G. S. Denisov, M. D. Toney and H.-H. Limbach, *J. Am. Chem. Soc.*, 2007, **129**, 6313–6327.

32 The experimentally observed thermodynamic preference for the complex **3·4b** ($\Delta G_{exp}$ (**3·3·4b** − **3·4b**) = −1.5 kJ) is qualitatively represented in the theoretical calculations, although by far less pronounced ($\Delta g_{theor}$ (**3·3·4b** − **3·4b**) = −12.2 kJ). Such a significant quantitative offset between experiment and computations was also found for CPA·imine systems and probably originates in dispersion interactions with the solvent (see ref. 15).

33 (*a*) E. J. Cabrita and S. Berger, *Magn. Reson. Chem.*, 2002, **40**, 122–127; (*b*) C. T. W. Moonen, P. van Gelderen, G. W. Vuister and P. C. M. van Zijl, *J. Magn. Reson.*, 1992, **97**, 419–425.

34 (*a*) S. Hoffmann, A. M. Seayad and B. List, *Angew. Chem., Int. Ed.*, 2005, **44**, 7424–7427; (*b*) M. Rueping, E. Sugiono, C. Azap, T. Theissmann and M. Bolte, *Org. Lett.*, 2005, **7**, 3781–3783; (*c*) R. I. Storer, D. E. Carrera, Y. Ni and D. W. C. MacMillan, *J. Am. Chem. Soc.*, 2006, **128**, 84–86; (*d*) G. Li and J. C. Antilla, *Org. Lett.*, 2009, **11**, 1075–1078; (*e*) A. Aillerie, V. L. de Talancé, A. Moncomble, T. Bousquet and L. Pélinski, *Org. Lett.*, 2014, **16**, 2982–2985; (*f*) X.-F. Cai, R.-N. Guo, G.-S. Feng, B. Wu and Y.-G. Zhou, *Org. Lett.*, 2014, **16**, 2680–2683; (*g*) Y. Zhang, R. Zhao, R. L.-Y. Bao and L. Shi, *Eur. J. Org. Chem.*, 2015, 3344–3351.

35 (*a*) M. R. Monaco, D. Fazzi, N. Tsuji, M. Leutzsch, S. Liao, W. Thiel and B. List, *J. Am. Chem. Soc.*, 2016, **138**, 14740–14749; (*b*) For a review including the crystal structure of the TRIP-dimer see: M. R. Monaco, G. Pupo and B. List, *Synlett*, 2016, **27**, 1027–1040.


This journal is © The Royal Society of Chemistry 2020